Journal of Sol-Gel Science and Technology (2026)119:45
https://doi.org/10.1007/s10971-026-07224-x

ORIGINALPAPER

The key to carbon aerogel microbeads: xanthan gum-mediated shape retention during gelation of resorcinol formaldehyde droplets

Thomas Anklam[1] · Seeni Meera Kamal Mohamed[1] · Philip Niemeyer[1] · Rebekka Probst[1] · Beruktayet Fekadu[2] · Frederic Kreps[2] · Marina Schwan[1] · René Tannert[1] · Barbara Milow[1]

Received: 14 November 2025 / Accepted: 20 July 2026

Abstract

Their high porosity, high surface area, and low density render resorcinol-formaldehyde (RF) aerogels attractive precursors to their carbon analogs which have interesting applications, for instance in adsorption, catalysis, or electrochemical energy storage. While they are conventionally produced by pyrolysis as monoliths in a laboratory scale, a large-scale production would be more facile if they were produced in the form of microbeads. The direct bead formation of RF solution by the dropping method is limited because of their inability to preserve the spherical shape until gelation due to the low viscosity of RF solution. Therefore, within this work, we aimed to improve the viscosity by adding the polysaccharide-based thickener xanthan gum (XG) to the RF solution and pre-gelling them, followed by dropping into an acid bath for rapid gelation. We were thus able to produce RF aerogel beads (RFB) and subsequently carbon aerogel beads (CB) with diameters ranging from 2.0–2.6 mm. Here, we investigated the physicochemical properties of the resulting RF and CB using various physicochemical techniques by varying the XG concentration and the type of acid gelation bath. N_2 physisorption analysis showed that CBs developed with high surface areas up to 1205 m^2/g, micropore volumes up to 0.43 cm^3/g and, bulk (tap) density of 0.31 g/cm^3. In order to evaluate the use of these CBs for applications such as carbon capture and electrode material, we furthermore investigated their CO_2 sorption capacity, electrical conductivity, and mechanical properties. These findings presented in this work demonstrate the promising potential of the carbon aerogel microbeads for such applications.

Graphical Abstract

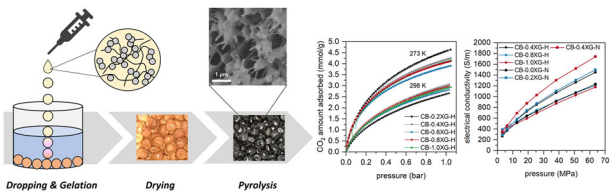

Keywords Aerogels · Resorcinol-formaldehyde · Xanthan gum · Carbon microbeads · Ultra-microporous · CO_2-adsorption · Electrical conductivity

✉ Seeni Meera Kamal Mohamed
seenimeera.kamalmohamed@dlr.de

✉ Barbara Milow
barbara.milow@dlr.de

[1] Department of Aerogels and Highly Porous Materials, Institute for Frontier Materials on Earth and in Space, German Aerospace Center (DLR), Cologne, Germany

[2] Department of Digitally Integrated Microstructure and Mechanics, Institute for Frontier Materials on Earth and in Space, German Aerospace Center (DLR), Cologne, Germany

Published online: 15 September 2026

Highlights

- The addition of xanthan gum facilitated the synthesis of RF aerogel microbeads via a dropping method.
- Pyrolysis of RF aerogel microbeads led to ultra-microporous carbon aerogel microbeads.
- Carbon aerogel microbeads exhibit surface areas up to 1206 m^2/g and micropore volumes up to 0.43 cm^3/g.
- CO_2 adsorption capacity of carbon aerogel microbeads is found to be 5.10 mmol/g at 1 bar and 273 K.
- Carbon aerogel microbeads have electrical conductivity up to 1740 S/m at 64 MPa.

1 Introduction

Over the last decades, various kinds of carbon nanomaterials such as activated carbon, carbon black, carbon nanotube, carbon microbeads, fullerene, graphene, natural graphite, and porous carbon (micro- and meso-) have received attention among researchers all over the world [1, 2]. Among these carbonaceous materials, carbon microbeads show interesting properties such as high thermal and chemical stability, high surface area, high porosity mainly comprised of meso- and micro-pores, high tap density, high thermal and electrical conductivity, etc. [3, 4]. These unique characteristics make them ideal candidate for many applications in adsorption and separation (air and water purification), CO_2 capture, catalysis, electrochemical energy storage (batteries and super capacitors), medicine (blood-cleansing), etc. [5–7]. Moreover, the production of carbon microbeads or microspheres will provide a broad use of these materials and also reduce the processing time, energy and equipment costs [8]. Several physical and chemical methods have been reported over the years for the preparation of carbon microbeads: physical methods for producing micrometer-sized carbon beads, such as decomposition of composite carbon rods from coal and nickel particles through arc-discharge or laser ablation technique, often resulting in low carbonization yield and requiring much energy [9, 10]. In contrast, chemical methods such as templating, chemical vapor deposition (CVD), and hydro- or solvo-thermal methods result in high carbonization yields and are less energy-intensive [10]. However, chemical methods still suffer from high costs and complexity in terms of the synthetic procedure involved. Nevertheless, both physical and chemical methodologies have been applied with low cost, and abundant polycyclic aromatic hydrocarbons, including coal tar, heavy oil, and pitch have been converted into carbon microbeads with high carbon content [10]. The most common procedure involves heating petroleum pitch or coal tar at 350–500 °C to produce mesophase spheres followed by quenching of carbonization, extraction, and separation of the spheres as solids with a suitable solvent. After an extensive growth and aggregation of the spheres, the carbonization yield is typically 5–10%. Besides the tedious extraction and the low carbonization yield of beads, a main drawback of this process is the uncontrollable bead size [11]. Carbon spheres were also prepared from different forms of pitches through sequential suspension procedures followed by solvent removal, filtration, and oxidative stabilization. Lü et al. [12] used coal tars with different primary pyridine insoluble fractions through heat treatment at 430–480 °C to form mesocarbon microbeads. Flame pyrolysis was also employed to form pyrolytic graphitic shells under elevated temperatures. The harsh conditions employed offer little to no control over the structure (bead composition, pore size, and diameter) [13, 14]. Carbon microbeads or microspheres have also been synthesized by an inverse-emulsion gelation method. In this method, micron-sized resorcinol-formaldehyde (RF) particles were produced in an oil-water emulsion followed by separation of wet particles, cleaning from residual oil, super-critical drying, and carbonization to achieve carbon microbeads or microspheres. This method involves large amounts of energy and long times during the washing and drying process because of the removal of the oil phase [15, 16]. Established methods for the synthesis of aerogel beads (mainly biopolymers such as cellulose, alginate, chitosan, and chitin) involve conventional dropping, vibrating nozzle, electrostatic forces, jet (mechanical) cutting, or spraying atomization [17]. A direct production of RF microbeads is difficult because of the low viscosity of the sol (~ 0.5 Pa·s) and fast gelation near to the gel point. However, several attempts were made to prepare spherical RF resin microbeads: Dwivedi et al. [18–20] produced spherical RF beads by the assistance of spherical divinylbenzene cross-linked polystyrene microspheres (XAD-4) and sodium alginate for the removal of cesium ions from radioactive wastes. Furthermore, RF foam shells with low density have been developed by microencapsulation techniques [21, 22]. However, all of these methods have to face the challenges of high costs and process complexity for large-scale production. Hence, it is essential to find an easy, direct and low-cost method to produce RF microbeads and their carbon counterparts.

Here, we report for the first time the direct shaping of RF solutions into microbeads by dropping them into an acid gelation bath and further carbonization to obtain carbon microbeads. The viscosity of the RF solution is improved by the addition of a polysaccharide-based thickener, xanthan gum (XG) to achieve sphericity. The properties of the RF and carbon beads were varied by changing the concentration of the thickener and the type of the acid gelation

bath (HCl & HNO_3). The produced RF microbeads (RFB) and carbon microbeads (CB) were characterized using different techniques such as pycnometry, attenuated total reflectance—Fourier transform infrared spectroscopy (ATR-FTIR), N_2-physisorption, TGA, WAXS, Raman spectroscopy, SEM, TEM, and uniaxial compression. Very importantly, the carbon microbeads were tested for their CO_2 sorption capacity and electrical conductivity in-order to demonstrate potential applications.

2 Experimental section

2.1 Chemicals and materials

Resorcinol (Sigma Aldrich, Germany), sodium carbonate (Sigma Aldrich, Germany), aqueous formaldehyde (23.5% w/w, Carl Roth, Germany), xanthan gum (XG, VT930, Deuteron GmbH, Germany), HCl solution (37%, PanReac AppliChem ITW Reagents, Germany) and aqueous HNO_3 solution (2 M, PanReac AppliChem ITW Reagents, Germany) were used without further purification. Deionized water was used throughout the experiments and obtained by passing tap water through an Enki Green-Line DIA 6000 MB purification cartridge (EnviroFALK, Westerburg, Germany).

2.2 Preparation of RFB

RFB was prepared as follows [23, 24]: Deionized water (W, 50.3 mL) was added to a 100 mL polypropylene screw-lid container pre-charged with resorcinol (R, 20.0 g), and the resulting solution was stirred with a magnetic stirring bar at 250 rpm for 10 min. After the addition of aqueous formaldehyde (F, 29.3 mL) solution (23.5%) and additional stirring at 250 rpm for 10 min, the solutions were thickened via addition of XG (0.2–1.0 w/v %). The catalyst Na_2CO_3 (C, 0.0128 g) was added in one portion, and stirring continued for another 40 min after homogeneous dispersion of XG. The pH values of the resulting solutions were typically ranging between 5.8 and 6.1. In some cases, pH values were adjusted to 5.4–5.6 (measured after additional stirring for 30 min) via addition of diluted 2 M HNO_3. The initial pH-values of RF solutions were measured using a SevenEasy pH-meter (Mettler-Toledo GmbH, Germany). Finally, the reaction containers were closed airtight and placed into a pre-heated drying cabinet at 60 °C for pre-gelation until the solutions were close to their gel points (determined by visual inspection of the appearance of turbidity). As the pre-gelation time was influenced by the position of the container inside the drying cabinet (Fig. S1), care was taken to place the reaction containers in the middle of the drying cabinet for the entire experiments. After pre-gelation, the containers were allowed to cool to ambient temperature by placing them in a water bath, and the pre-gelled RF solutions were subsequently transferred into a syringe or a pressurized container (Fig. S2), to which blunt-tip Sterican cannulas (B. Braun Melsungen, Germany) with a length of 22 mm and a diameter of 0.8 mm were attached. The RF solutions were added drop-wise into the acidic (2 M HCl or 0.5 M HNO_3) gelation bath from such syringe or pressurized container, and the resulting RF-gel microbeads were filtered after their color changed to pink (Fig. S3) and placed in a closed container in the drying cabinet at 60 °C for 1 d for curing. The cured beads were washed with deionized water until the pH of the washing liquid was neutral and subsequently dried in a drying cabinet at 60 °C. Throughout all the experiments, reagent stoichiometric ratios were set to R/C = 1500, R/F = 0.74, and R/W = 0.044, resulting in a total mass concentration (M_{RF}) of 27% [25]. Generally, samples were labeled as follows: in case of samples resulting from applying initial pH adjustment with 2 M HNO_3, "a" is added after "RFB" and "CB". The employed amount of XG is noted with "XG" together with the used concentration in wt% as prefix. The gelation baths were referred to as "H" for 2 M HCl and "N" for 0.5 M HNO_3. For instance, RFB synthesized without pH-adjustment using 0.2 wt% XG and 2 M HCl as gelation bath is referred to as "RFB-0.2XG-H" and the same sample with pH-adjustments is referred as "RFBa-0.2XG-H".

2.3 Preparation of CB

The carbonization of RFB was carried out in ceramic crucibles in a tube furnace (⌀ = 150 mm, l = 500 mm, Gero Hochtemperaturöfen GmbH, Germany) by heating to 1000 °C with a heating rate of 400 K/h at 50 mbar after purging with Ar three times, followed by holding the temperature for 1 h and letting the furnace cool down to temperatures between 30 and 50 °C. The carbonization yields were calculated as percentage ratios of masses before and after the carbonization.

2.4 Methods

2.4.1 Drying cabinets for gelation, curing and drying

The gelation, curing, and drying of RFB was performed at 60 °C in UF30 or UF110 drying cabinets (Memmert GmbH + Co. KG, Germany).

2.4.2 Determination of bead diameter

The average diameter of RFB and CB was measured for 100 beads of each batch using a digital sliding calliper.

2.4.3 Density

The tapped densities were measured by weighing 2 cm^3 of RFB or CB in a measuring flask after forming a close packing by tapping. The skeletal densities were measured using an AccuPyc II 1340 helium pycnometer (Micromeritics GmbH, Germany). The purge- and cycle fill pressure was set to 19.500 psig, and a pressure change rate of <0.0050 psig/min was set as an equilibrium condition. The samples were purged 10 times in case of RFB and 30 times in case of CB and measured 10 times in both cases.

2.4.4 Porosity

The porosities (P) of RFB and CB were calculated using the following equation, where ρ_t and ρ_S represent the tapped density and skeletal density, respectively.

$$P(\%) = 1 - \left(\frac{\rho_t}{\rho_s}\right) * 100$$

2.4.5 Physisorption experiments (N_2, Kr and CO_2)

The Brunauer-Emmett-Teller (BET) surface area and micropore volume of the microbeads were derived from the N_2 physisorption isotherms, measured using a 3Flex physisorption analyser (Micromeritics GmbH, Germany) at a temperature of 77.3 K. In case of RFB, the isotherms were measured by increasing the relative pressure in $\Delta p/p^0 = 0.025$ steps until a final relative pressure of $p/p^0 = 0.300$. In case of CB, the isotherms were measured by first increasing the relative pressure with N_2 dose amount increments of 0.35692 mmol/g until a relative pressure of $p/p^0 = 0.010$ was reached. Afterward, the relative pressure was increased in $\Delta p/p^0 = 0.025$ steps until a final relative pressure of $p/p^0 = 0.400$. The micropore volume of the CB was calculated from t-plots using carbon black statistical thickness surface area (STSA) as reference data (from Micromeritics GmbH, Germany). The micropore size distributions of CB were calculated using the HS-2D-NLDFT model (slit pore geometry). In some cases, BET surface areas of RFB were additionally investigated with Kr-physisorption at 77.1 K by increasing the relative pressure to $p/p^0 = 0.060$ in the first step followed by an increase in $\Delta p/p^0 = 0.020$ increments until a final relative pressure of $p/p^0 = 0.200$. All the measurements were analyzed with MicroActive Version 6.00 (Micromeritics GmbH, Germany). CO_2 adsorption capacities of CB were derived from CO_2 sorption isotherms that were measured using a TriStar II 3020 physisorption analyzer (Micromeritics GmbH, Germany) at 273 and 298 K. The relative pressure was increased in $\Delta p/p^0 = 0.00050$ steps until a final relative pressure of $p/p^0 = 0.030$ for measurements at 273 K and in $\Delta p/p^0 = 0.00025$ steps until a final relative pressure of $p/p^0 = 0.016$ for measurements at 298 K. Prior to the measurements, RFB and CB were outgassed under vacuum conditions ($2.67 \cdot 10^{-3}$ kPa) at 120 °C for 12 h and 200 °C for 12 h, respectively, using a Smart VacPrep 067 HIVAC device (Micromeritics GmbH, Germany). The IUPAC recommendations for the application of the BET method to microporous materials have been taken in consideration for all measurements [26].

2.4.6 ATR-FTIR

Attenuated total reflectance—Fourier transform infrared spectroscopy (ATR-FTIR) spectroscopy was performed on a Tensor 27 spectrometer (Bruker Optics GmbH & Co. KG, Germany) measuring a total of 150 scans over a spectral range of 4000–400 cm^{-1} with a resolution of 4 cm^{-1}, for each sample. Prior to each measurement the background was measured. For each measurement, the baseline was corrected (concave rubberband method, 5 iterations) using OPUS 7.0 Software (Bruker Optics GmbH & Co. KG, Germany).

2.4.7 Raman spectroscopy

Raman spectroscopy was performed on a XploRA Plus Raman microscope (HORIBA Europe GmbH, Germany) using a laser wavelength of 532 nm.

2.4.8 Wide angle X-ray scattering

Wide angle X-ray scattering (WAXS) measurements were performed on a D8 Advance diffractometer (Bruker Corporation, USA) using Cu Kα radiation ($\lambda = 0.15406$ nm) operating the X-Ray tube at 35 kV and 30 mA. The microbeads were ground with an agate mortar, and the powder was placed on a Si single crystal with a pit of 5 mm diameter and 0.8 mm depth. The processing of raw data was done with the EVA-program and compared with the databases of ICDD-PDF2 (2019) and BRUKER COD (2020). The crystallite size D was calculated using Scherrer equation ($D = \frac{K \cdot \lambda}{\beta \cdot \cos\theta}$). A value of 0.90 was used for the shape factor K. The full width at half maximum of the peak (β) was determined using Origin software by performing manual base line correction and using the peak analysis tool.

2.4.9 Scanning electron microscopy

The microstructures of the samples were analyzed using an ULTRA55 scanning electron microscope (Carl Zeiss AG, Germany) at an operating voltage of 2 kV. A thin platinum layer was sputtered with a SCD 500 Sputter Coater (BalTec

AG, Switzerland) on all samples from the top for 60 s with a current of 21 mA. RFBs were additionally sputtered from two opposite sites for 45 s with a current of 21 mA before the measurements. The particle size was estimated with linear intercept method.

2.4.10 Transmission electron microscopy

For the nanostructure analysis of CBs, a Tecnai F30 transmission electron microscope (Philips, Netherlands) was used with an acceleration voltage of 300 keV. To provide thin enough samples, 80 nm slices were produced with a Powertome ultramicrotome (RMC Boekeler, USA) and collected on copper R2/1 omniprobe TEM grids. To stabilize the material for the ultramicrotome preparation, CBs were embedded beforehand in EMbed812 epoxy resin (Electron Microscopy Science, USA) [27]. Since this is a new sample preparation approach for aerogels, a conventional powder preparation was done for one sample serving as a control. The TEM images were processed using Gatan Digital Micrograph in-order to obtain the Fourier Transform (FT) images.

2.4.11 Determination of electrical conductivity

The electrical conductivity of CB microbeads was investigated using a resistivity measurement system (PD-51, Loresta GX, Mitsubishi Chemical Europe). The system is based on the 4-pin measuring method of surface resistance at constant pressures between 1 and 10 kN [28]. The device was filled with a bed of CB microbeads for each measurement.

2.4.12 Mechanical testing

The quasi-static compression tests of the carbon microbeads (diameter of ~2.0 mm) were performed using a universal testing machine (Instron GmbH, Germany) with a 50 N load cell at a displacement rate of 1.0 mm/min. The tests aimed at finding out the maximum compressive force at which the CBs break. Each set of compressive tests was carried out using at least four different CBs.

3 Results and discussion

3.1 Development of dropping process

RFB and CB were synthesized according to the procedure described in the experimental section, using XG concentrations ranging between 0.0–1.0 wt%. The pre-gelation time decreased with an increasing concentration of XG, and the pH-modified RF solutions (RFBa) required longer pre-gelation time, corresponding to a report by Job (Table S1) [29]. For dropwise addition to the gelation bath, the distance between the tips of the cannulas and the surface of the gelation bath was adjusted between 5–10 cm in order to achieve spherical beads with minimal deformation. The average diameter of RFB and CB and the respective gravimetrical carbon yields after carbonization are summarized in Table 1.

Table 1 Average bead diameter of RFB-XG-H, RFB-XG-N, CB-XG-H, and CB-XG-N and their respective carbonization yields

XG conc. (w/v%)	Acid	Average diameter (mm)		Carbon yield (mass%)
		RFB	CB	
0.2	H	2.2 ± 0.2	1.8 ± 0.1	42.8
0.6	H	2.3 ± 0.1	1.75 ± 0.08	35.3
1.0	H	2.6 ± 0.3	2.0 ± 0.2	43.2
0.2	N	2.4 ± 0.2	1.9 ± 0.1	44.2
0.6	N	2.4 ± 0.2	1.8 ± 0.2	43.3
1.0	N	2.2 ± 0.2	1.7 ± 0.2	44.3

The average diameter of thus obtained beads was 2.2–2.6 mm for RFB-XG-H samples and 2.2–2.4 mm for RFB-XG-N samples. After carbonization, the diameters shrunk to 1.8–2.0 mm for CB-XG-H and 1.7–1.9 mm for CB-XG-N. The gravimetrical carbon yields after carbonization were ranging between 35.3 and 43.2 mass% for RFB-XG-H and 43.3–44.3 mass% for RFB-XG-N. The trend in the diameters of the RFB and CB are quite similar for the pH-modified system. However, gravimetrical carbon yields after carbonization were higher in case of the pH-modified system (Table S2). The pre-gelled RF solutions prepared without XG resulted in irregularly shaped solids instead of spherical beads (Fig. S4). RFB appear slightly more dented with increasing XG concentration and generally kept their shape upon carbonization (Fig. 1).

3.2 Density

The tapped density, skeletal density, and porosity of the RFB and CB samples are summarized in Table S3. The skeletal densities of RFB without XG ranged between 1.42–1.48 g/cm^3, which is in accordance with values typically reported for RF aerogels [30–32]. In the case of RFB-XG-H, skeletal densities were, with the exception of RFB-0.6XG-H (1.32 g/cm^3), ranging between 1.39–1.43 g/cm^3. The skeletal densities of CB derived from RFB-XG-H samples (CB-XG-H) were ranging between 2.03–2.36 g/cm^3 which is in good agreement with the values reported for carbon monolithic aerogels [25]. The tapped densities of RFB-XG-H and CB-XG-H were ranging between 0.17–0.29 and 0.21–0.28 g/cm^3, respectively. The XG concentration did not influence the tapped densities.

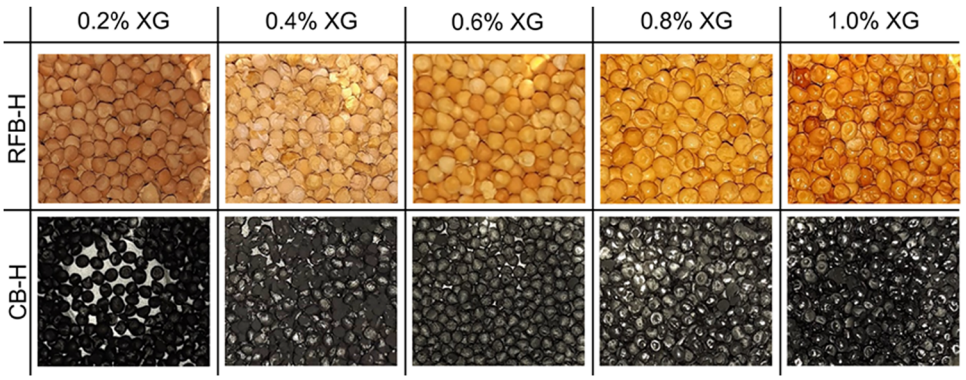

Fig. 1 Influence of XG concentration on the shape of the resulting RFB-XG-H and CB-XG-H samples

According to reported literature [30, 33], the bulk densities of monolithic RF aerogels produced with base-acid catalysis and its monolithic carbon aerogels typically vary between 0.24 g/cm^3 and 0.34 g/cm^3. In the case of using aqueous HNO_3 solution instead of HCl solution as gelation bath, the skeletal densities of RFB-XG-N and CB-XG-N were in the range of 1.39–1.42 g/cm^3 and 2.19–2.30 g/cm^3, respectively, which are typical values for RF and their carbon aerogels [25, 31]. The tapped densities of RFB-XG-N and CB-XG-N were ranging between 0.22–0.31 and 0.19–0.26 g/cm^3, respectively. The density values are similar to the values for samples dropped in HCl and, again, do not correlate with the XG concentration. The trend and values for RFB and CB produced with HCl and HNO_3 after pH modification showed similar behavior as discussed above (Table S3). Therefore, neither XG concentration, nor pH adjustment before pre-gelation significantly influenced skeletal density and tapped density.

3.3 Porosity

The porosities of RFB-XG-H and CB-XG-H ranged between 78–88 and 86–92%, respectively. The XG concentration has no influence on the porosity. However, CB-XG-H samples have a higher porosity than their RFB-XG-H precursors. The porosities of RFB-XG-N and CB-XG-N ranged between 78–84 and 89–92%, respectively. Again, CB-XG-N samples have a higher porosity than their corresponding RFB-XG-N precursors. The porosities are also in the same region as for all RFB-XG-H and CB-XG-H samples. The trend and values for RFB and CB produced with HCl and HNO_3 after pH modification showed similar behavior as discussed above (Table S3). Therefore, neither XG concentration, nor pH adjustment before pre-gelation significantly influenced porosity.

3.4 Chemical structure

The chemical structure of RFB and CB was investigated with ATR-FTIR spectroscopy (Figs. S5–S8). The spectra of RFB samples are in good agreement with the literature [28, 34], and the disappearance of the majority of the bands in case of CB samples confirms the successful carbonization and also the removal of oxygen containing functional groups. ATR-FTIR spectra of all RFB have the same absorption bands regardless of pH adjustment or the acid used. The band at 3382 cm^{-1} has been assigned to the phenolic -OH stretching vibration, bands at 2942, 2874, and 1479 cm^{-1} have been assigned to the -CH_2 stretching and scissoring vibrations of methylene bridges, respectively, and the bands at 1222 and 1092 cm^{-1} have been assigned to the -C-O-C- stretching vibrations of methylene ether bridges. The reference spectrum of XG shows absorption bands at 3309, 1606, 1400, 1370, 1238, and 1016 cm^{-1}, which is in accordance with the reported values [35]. The overlapping of the characteristic bands of RF and XG are expected as both contain methylene and alcohol groups. However, XG has a band at 1016 cm^{-1} (deformation of primary alcohol C-O) which doesn't overlap with the RF spectrum and doesn't appear in the RFB-XG-H spectra. It is therefore concluded from ATR-FTIR spectra that the addition of XG additive does not influence or hinder the polycondensation of the precursors and thus the formation of RF aerogel. CB-XG-H samples show only a general low transmittance without sharp absorption bands. This confirms that CB samples do not contain any significant amount of residual functional groups from RF or XG. The spectra of all samples exhibit the same bands, irrespective of XG concentration, gelation bath, and pH adjustment (Figs. S5-S8). The WAXS measurements on CB are presented in Figs. 2a and S9. The WAXS pattern of CB-0.6XG-H (Fig. 2a) is in accordance with carbon aerogel diffractograms reported in the literature [25, 36]. The intensity maxima in the pattern are related to scattering of short range structures rather than to diffraction in ordered graphite. The broadness of the observed intensity maxima between 10 and 60° is typical for partly graphitized carbon [37]. The diffractogram shows three different maxima at 22.4°, 43.7°, and 79.9°. The maximum at 22.4° results from interlayer scattering between parallel-stacked graphenic

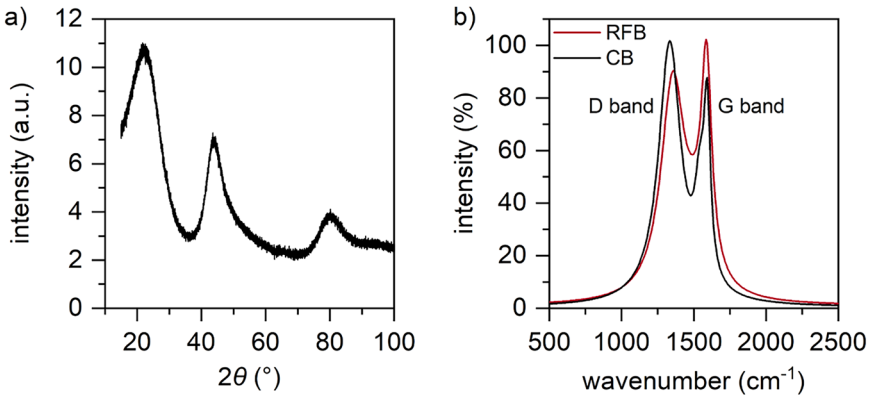

Fig. 2 **a** WAXS pattern of CB-0.6XG-H and **b** Raman spectra of RFB-0.6XG-H and the respective CB-0.6XG-H

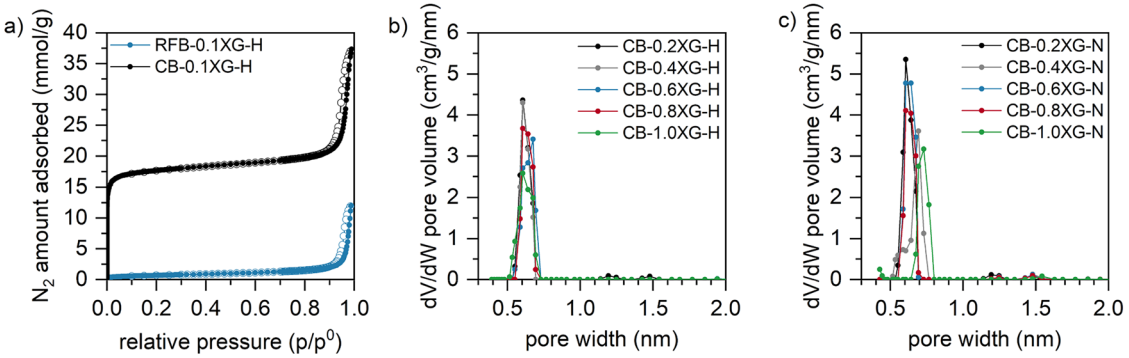

Fig. 3 **a** Representative N_2 sorption isotherms of RFB-0.1XG-H and CB-0.1XG-H measured at 77.3 K. Filled circles refer to the adsorption branches of the isotherms and empty circles refer to the desorption branches of the isotherms. **b** HS-2D-NLDFT micropore size distribution of CB-XG-H and **c** HS-2D-NLDFT micropore size distribution CB-XG-N with varying XG concentrations

nanoregions, and the other two maxima result from scattering at the atoms of the first and second coordination sphere of graphenic nanoregions. The WAXS patterns are quite similar for all types of CBs produced irrespective of the initial pH and acid used (Fig. S9). The crystallite size was calculated with Scherrer's equation using the peak at 79.9° for each sample. The domain size was 2–3 nm for CB-06XG-H, CBa-0.6XG-H, CB-0.6XG-N and CBa-0.6XG-N. The very small domain size indicates a mainly amorphous carbon structure with graphenic nanocrystallites.

The structural evolution of CB from RFB was analyzed using Raman spectroscopy (Fig. 2b). RF beads exhibit two bands at 1354 and 1583 cm^{-1} with relatively different strengths. The D-band (A_{1g} symmetry) of the RF beads at 1354 cm^{-1} resulted from the sp^3-hybridized carbon system that gives rise to flaws in the graphene crystal structure. The sp^2-hybridized carbon or graphene structure related to the G-band (E_{2g} symmetry) of the system appeared at 1583 cm^{-1} [38, 39]. CBs have analogous bands at 1334 and 1591 cm^{-1} related to D- and G-bands, respectively. The D-band is assigned to the defects present in the carbon structure of carbon beads. These defects present in the carbon structure determine the active sites responsible for the adsorption of gases, especially CO_2. The G-band was assigned to the sp^2 hybridized carbon present in the structure. The degree of graphitization (I_D/I_G) as a measure of disorder is calculated using the intensity ratios of D- and G-bands. The I_D/I_G values for the RFB and CB are found to be 1.03 and 1.35, respectively. It is clearly evident from the increase of I_D/I_G value that the ordered carbon arrangement of RF network starts to break, thereby increasing the content of disordered carbon. This distortion creates defects in the structure of the carbon beads, as well as micropores. Such defects and micropores could enhance CO_2 adsorption capacity of the carbon materials [39, 40].

3.5 Surface area, pore size distribution and pore volume

The representative N_2 adsorption/desorption isotherms of RFB and CB are depicted in Fig. 3a. According to IUPAC classifications, the isotherm of RFB exhibits characteristics of type II and type IV(a) isotherms, indicating the presence of macro- and mesopores (see SEM images) and the absence of micropores [26, 31]. The isotherm of CB exhibits pronounced characteristics of type I(a) isotherms,

Table 2 BET surface area, micropore surface area and *t*-plot micropore volume for CB-XG-H and CB-XG-N synthesized with varying XG concentrations

Sample	BET surface area (m^2/g)	micropore surface area (m^2/g)	*t*-plot micropore volume (cm^3/g)
CB-0.2XG-H	977 ± 3	900	0.35
CB-0.4XG-H	867 ± 2	783	0.30
CB-0.6XG-H	956 ± 1	861	0.33
CB-0.8XG-H	909 ± 2	846	0.33
CB-1.0XG-H	784 ± 3	734	0.28
CB-0.2XG-N	1176 ± 4	1098	0.42
CB-0.4XG-N	912 ± 1	848	0.32
CB-0.6XG-N	1206 ± 1	1121	0.43
CB-0.8XG-N	1041 ± 3	967	0.37
CB-1.0XG-N	858 ± 1	824	0.31

revealing the highly microporous nature of CBs and narrow width of micropores (< 1 nm), as well as some type IV isotherm characteristics which are typical for mesoporous materials [25, 26].

BET analysis of the N_2 and Kr isotherms of RFB revealed specific surface areas below 35 m^2/g, in some cases even as low as 7 m^2/g (Table S4), which is in good agreement with RFB-H and other base-acid catalyzed monolithic RF aerogels [30]. However, CB-XG-H samples have specific surface areas ranging between 785 and 978 m^2/g which is on par with the values reported for monolithic carbon aerogels (Table 2) [25, 41]. The addition and increase of XG concentration do not have any significant influence on the surface area of either RFB and CB. As evidenced from ATR-FTIR, XG apparently only acts as a viscosity modifier and is not involved in any chemical reaction or bonding. CB samples have much higher surface area compared to their parent RFB as the carbonization process induces micropore formation [41]. The extent of micropore contribution is dominating the total surface area as indicated by the ratio of external- and micropore surface area for CB-XG-H samples irrespective of their XG concentrations. In case of CB-XG-H samples, 735–901 m^2/g of the total surface area are contributed by micropores whereas only 50–95 m^2/g resulted from the external surface of the carbon beads. The micropore volume ranges from 0.28–0.35 cm^3/g without any correlation to the XG-concentration which is in good agreement with the micropore volume reported for similar kinds of carbon aerogels in the range between 0.20 and 0.22 g/cm^3 (Table 2) [25]. In the case of RFB produced using HNO_3, BET surface areas ranged between 14 and 26 m^2/g, similar to beads produced using HCl (Table S2). Upon carbonization, the BET surface area of CB-XG-N is increased to 856–1206 m^2/g, which is significantly higher than that of HCl samples (Table 2). As expected, the XG concentration does not influence surface area. Again, micropore surface area (825–1122 m^2/g) contributes most to total surface area, irrespective of the XG concentration.

Generally, CB-XG-N samples have larger BET surface areas and pore volumes than CB-XG-H samples. As discussed in the experimental section, 0.5 M HNO_3 was used as the regeneration medium for the bead formation. We washed the RF beads after regeneration and curing at 60 °C using distilled water until neutral pH was apparent. However, there might be possibilities of some residual acids present in the pores of the RFB. During the carbonization process, HNO_3 can activate the carbon and enhance its surface area, porosity and other properties which was reported earlier [42, 43]. The use of elevated temperature (1000 °C) during the pyrolysis of RFB along with HNO_3 might have caused oxidation and nitration of the carbon surface in a similar way [43, 44]. The diffusion of HNO_3, which may act as an oxidant, into the pores of the carbon formed during the pyrolysis may increase the amount of micropores. This greatly enhances the gas-adsorbing capacity of CB adsorbent by improving its ion-exchanging capacity [44]. The micropore volume of CB-XG-N ranged between 0.31–0.43 cm^3/g which is also independent of the XG concentration. As similar to surface area, micropore volume is higher for HNO_3 samples compared to HCl samples. The HS-2D-NLDFT pore size distributions of CB-XG-H with different XG concentration are displayed in Fig. 3b. According to IUPAC guidelines for type I(a) materials, CB-XG-H samples have narrow pore size distributions (ultra-micropores) of widths ranging between 0.5 and 0.7 nm with a negligible amount of additional pores of 1.2 and 1.5 nm width in the case of CB-0.2XG-H. The concentrations of XG doesn't influence the micropore width. Figure 3c shows the HS-2D-NLDFT pore size distribution of CB-XG-N samples with varying XG concentrations. The micropore size is quite similar to other carbon aerogels ranging between 0.5 and 2.0 nm [25]. All samples show a high amount of ultra-micropores with widths ranging between 0.5–0.8 nm and a small contribution of pores with a width of 1.2 and 1.5 nm. The pore size distributions are similar to the distributions found for HCl samples and again, are not influenced by XG concentration.

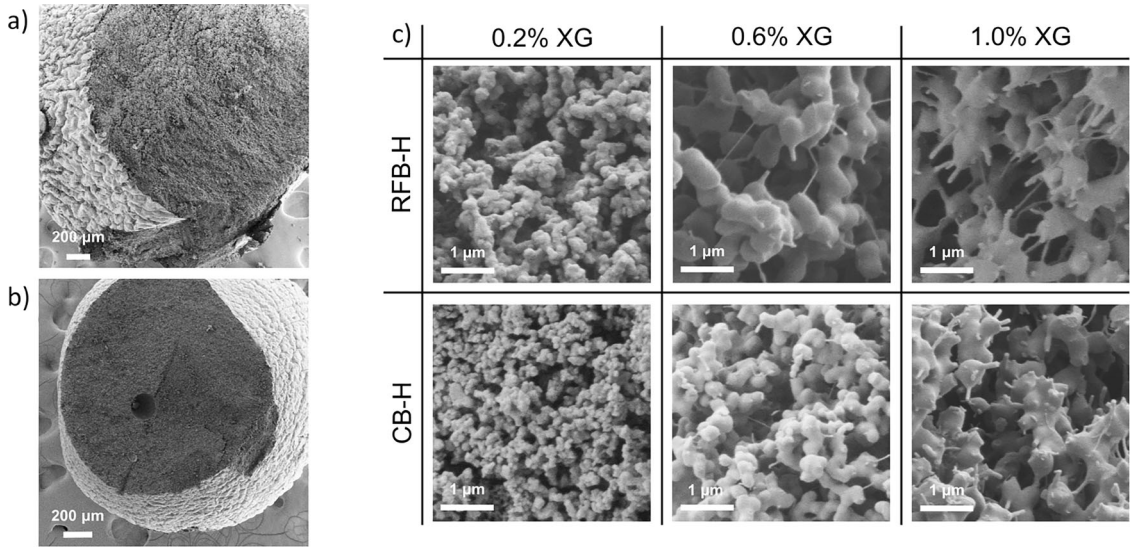

Fig. 4 SEM micrographs of the cross-section of **a** RFB-0.6XG-H and **b** CB-0.6XG-H and **c** the inner microstructure of RFB-XG-H samples with varying XG content and the respective CB-XG-H samples

Furthermore, the pH-adjustment resulted in similar pore-size distributions and micropore volumes (Fig. S10, Table S4).

3.6 Micro- and nanostructure morphology

The morphology and microstructure of RFB-XG-H and CB-XG-H samples were investigated by means of SEM on surfaces which were generated by splitting the beads with a sharp blade. Both RFB-XG-H and CB-XG-H display a dense skin on the external surface of the beads (Fig. 4a–b). The inner microstructures of RFB-XG-H with varying XG concentration and the respective CB-XG-H samples are generally composed of nearly spherical particles with a size of few hundred nanometers that are connected to each other via broad necks, creating a 3-dimensional open network with macro-pores in the size range of few micrometers (Fig. 4c). The size of the nanoparticles has been estimated manually by linear intercepts of particle contours for CB samples (Table S5). This subjective method has been used since the particles are agglomerated and interconnected and therefore hardly discernible by automated image analysis. The most significant alteration of the microstructure was related to the concentration of XG. Without addition of XG the nanoparticles were much smaller than with XG addition (compare Fig. S11 and Figs. 4, S12–S14). With increasing XG content, fibrous appendices to the nanoparticles formed. With increasing XG content, the number of fibrous appendices increases, forming connections between nanoparticles, especially in the case of high XG contents of 1.0 wt%. This might furthermore indicate that the trend of shortened periods required for pre-gelation was related to a quicker percolation process as the XG concentration increased. Comparing RF and CB samples, the nanoparticle size was slightly smaller and the number and length of fibrous appendices was less in CB samples. In the case of the RFBa-H and CBa-H samples with 0.6 wt% the nanoparticles in the CBa sample were slightly larger. The microstructures of CB samples which were synthesized with initial pH adjustment were quite similar to those without pH adjustment, but for lower XG concentrations of 0.2 wt% the nanoparticles in pH adjusted samples were larger, (Fig. 4, S12–S14, Table S5). The increase of particle size with adjusting pH is in good agreement with the particle morphology reported for a base-acid catalyzed route by Laskowski et al. [30]. Laskowski et al. [30] observed that the addition of acid (1.5 h after the start of the sol-gel reaction) to the base catalyzed solution induces fast condensation of the existing RF particles, leading to them being covered by an RF layer produced in the acid catalyzed step which increased the average particle size to 2.2 µm.

For TEM analysis, in order to prevent overlapping of particles, samples were prepared by embedding in EMbed 812 and slicing using an ultramicrotome [27]. A comparison with a sample prepared by a conventional powder method (Fig. S15a–d) demonstrated the suitability of the ultramicrotome method (Fig. S15e–h) for the preparation of aerogels. With this preparation method, particle overlap is less pronounced so that a comparison of the porosity and morphology between different samples is easier. On the other hand, the contrast provided by the embedding material makes it sometimes difficult to discern between embedding material and particles. However, all analyzed samples were prepared with the embedding and ultramicrotome slicing method. TEM micrographs of a)

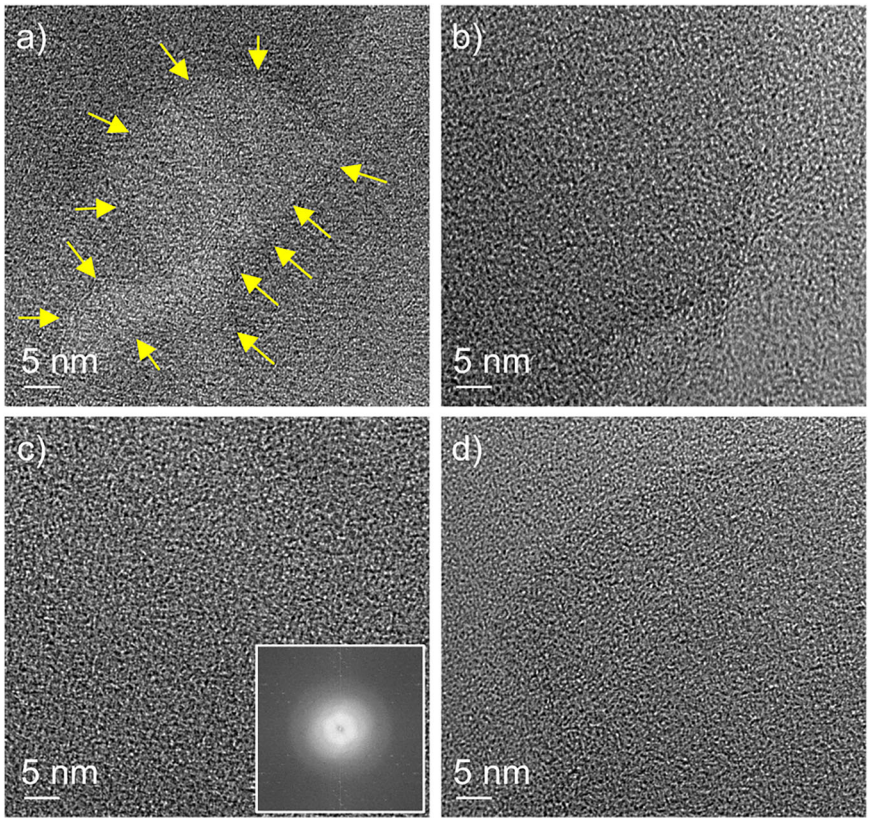

Fig. 5 TEM micrographs of **a** CB-0.2XG-H, **b** CB-0.2XG-N, **c** CB-0.6XG-N, and **d** CB-0.6XG-H. The inset in **c** displays an image of Fourier transform (FT) analysis of the respective TEM image. All TEM micrographs show 80 nm thick slices of overlapping carbonized particles. A pore within the slice of **a** is marked with yellow arrows. Pixel size of the micrographs is 57 pm

CB-0.2XG-H, b) CB-0.2XG-N, c) CB-0.6XG-N, and d) CB-0.6XG-H are shown in Fig. 5. The pixel size of the images taken at the highest magnification is 57 pm, which allows long range graphitic layer structures to be discerned with typical spacing of 340 pm. As such patterns are not observed in TEM images and Fourier transform (FT) showed no significant reflections (exemplary inset in Fig. 5c), it can be concluded that the samples have mainly an amorphous structure along with short-range ordered graphitic structure, as reported for similar carbon materials [45, 46]. Such amorphous structure with some graphitized micro regions is in line with the WAXS patterns discussed before (Fig. 2a). Additional TEM images at different magnifications are shown in Figs. S15–S17. TEM analyses reveal similar morphology and microporosity for all analyzed CB samples, irrespective of XG concentration and type of acid used for the gelation bath. At low magnification all samples display partly interconnected submicron sized particles of about 200–300 nm as shown for typical samples in Fig. S15a, b, e, and f.

3.7 CO_2 sorption capacity

The CO_2 sorption capacity of the carbon microbeads have been investigated using CO_2 adsorption/desorption isotherm at 273 and 298 K as the CBs have significant micro-porosity (Fig. 6). All the carbon microbeads have micropores below 1 nm which are responsible for their CO_2 capacities at ambient pressure [47]. As seen from HS-2D-NLDFT pore size distribution graphs (Fig. 3b, c), some carbon microbead samples have additional pores in the size above 1 nm. Table S6 provides the CO_2 sorption capacity of carbon microbead samples at two different temperatures (273 and 298 K) and different pressures of 1 bar and 0.1 bar. CB-XG-H samples are found to have CO_2 capture capacities ranging from 3.87–4.57 cm^3/g at 273 K and 2.77–2.97 cm^3/g at 298 K at 1 bar. The CO_2 adsorption capacity at low pressures of 0.1–0.15 bar is crucial as it indicates the real CO_2 partial pressure in the flue gas [48]. The carbon microbeads produced using HCl are found to have CO_2 capture capacities ranging from 1.43–1.49 cm^3/g at 273 K and 0.66–0.80 cm^3/g at 298 K under 0.1 bar. Among all the CB samples from HCl, CB-0.2XG-H has the highest CO_2 uptake of 4.57 and 1.46 mmol/g at 273 and 298 K at 1 bar, respectively, which is attributed to it having the highest micropore volume of 0.35 cm^3/g. The good CO_2 adsorption capacity is mainly because of the developed ultra-micropores below 1 nm. The CO_2 adsorption capacity of pH-modified CB samples (CBa-XG-H) was found to be in the range of 3.98–4.55 mmol/g at 273 K and 2.76–3.04 mmol/g at 298 K at 1 bar. whereas the CO_2 sorption capacity at 0.1 bar is in the range of

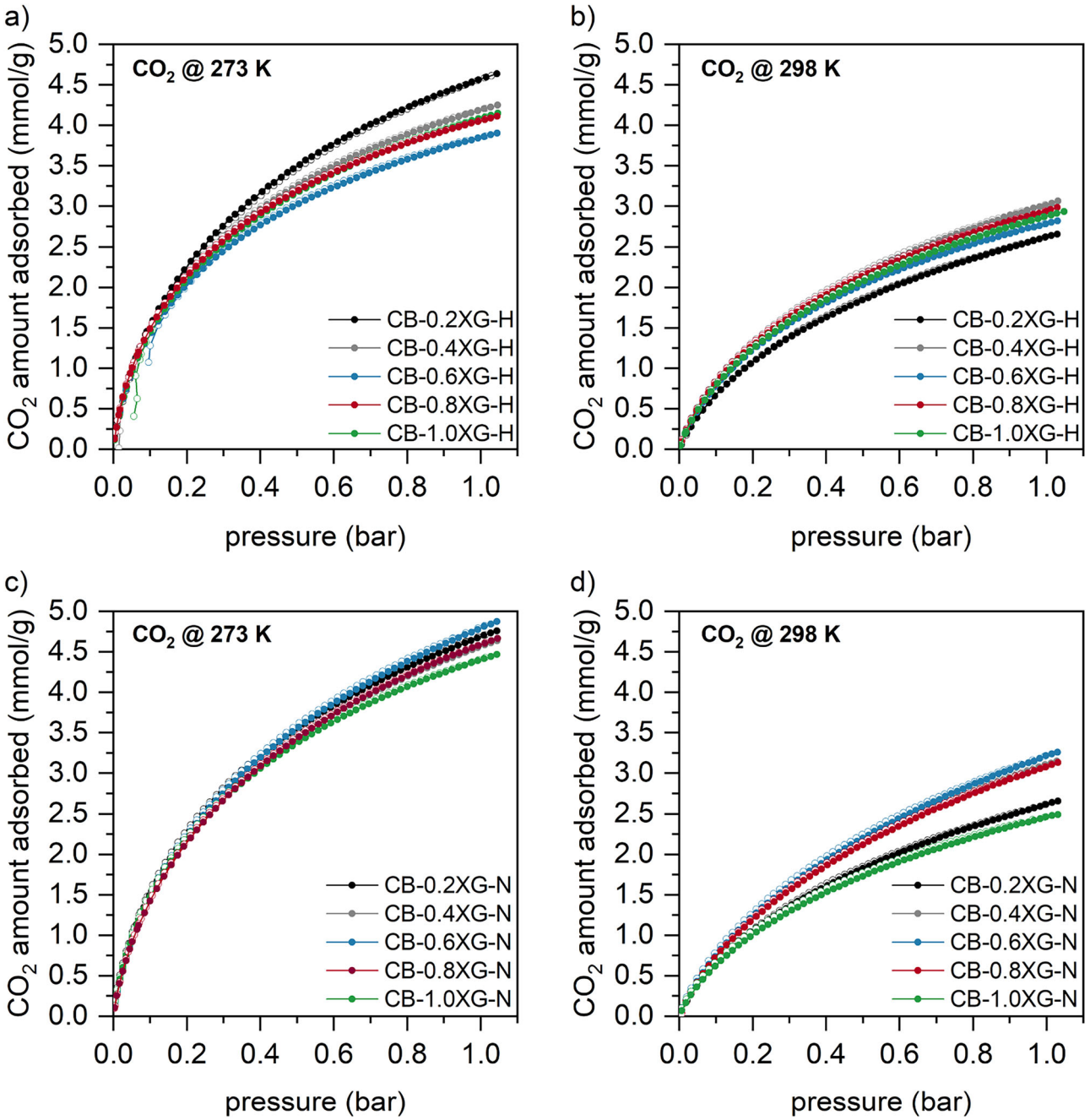

Fig. 6 CO_2 sorption isotherms of **a** CB-XG-H measured at 273 K, **b** CB-XG-H measured at 298 K, **c** CB-XG-N measured 273 K and **d** CB-XG-N measured at 298 K with XG concentrations of 0.2% (black), 0.4% (gray), 0.6% (blue), 0.8% (red) and 1.0% (green). Filled symbols denote measurement points of the adsorption branches and empty symbols denote measurement points of desorption branches of the isotherms

1.46–1.61 mmol/g at 273 K and 0.78–0.84 mmol/g at 298 K (Fig. S18, Table S6).

The change of regeneration bath from aqueous HCl solution to aqueous HNO_3 solution for the production of RF and its carbon microbeads greatly increased its micropore volume to a value of 0.43 cm^3/g for the sample CB-0.6XG-N. As already mentioned, the presence of HNO_3 might cause nitration, oxidation and activation of the carbon microbead samples at elevated temperatures and thereby increase micro-porosity [44]. CBs prepared using HNO_3 have CO_2 sorption capacity in the range of 4.41–4.81 mmol/g at 273 K and 2.98–3.09 mmol/g at 298 K under 1 bar. In the case of lower pressure of 0.1 bar, the CO_2 sorption capacity is found to be 1.44–1.53 mmol/g at 273 K and 0.70–0.76 mmol/g at 298 K. The sample, CB-0.6XG-N has the highest CO_2 sorption capacity of 4.81 mmol/g which is

in good correlation with the higher amounts of micro-porosity (0.43 cm^3/g). The pH-modified beads (CBa-XG-N) produced with HNO_3 have CO_2 sorption capacity of 3.76–5.12 mmol/g at 273 K and 2.73–2.94 mmol/g at 298 K under 1 bar. In the case of a lower pressure of 0.1 bar, the CO_2 sorption capacity is found to be 1.31–1.80 mmol/g at 273 K and 0.05–0.81 mmol/g at 298 K (Fig. S18, Table S6). Overall, the CO_2 sorption capacity is independent of XG concentration and greatly dependent on the micropore amount. The CO_2 sorption capacity of the carbon beads is in good agreement with the values reported for phenolic resin derived carbons [46, 49]. The overall performance of the adsorbents is mainly characterized by their surface area, micro-porosity, and bulk density. We have developed carbon bead adsorbent with high surface areas up to 1205 m^2/g and micropore volume of 0.43 cm^3/g with bulk (tapped) density up to 0.31 g/cm^3 and achieved a highest CO_2 adsorption capacity of 4.81 mmol/g at 273 K at 1 bar.

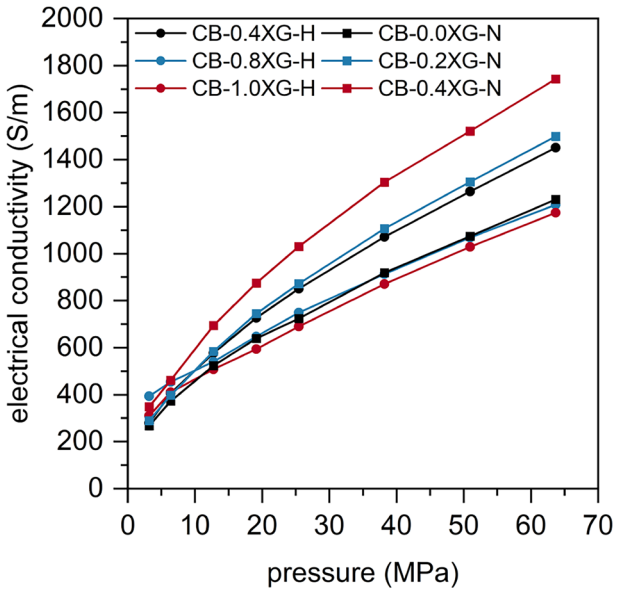

Fig. 7 The 4-point-measurement electrical conductivities of CB-XG-H and CB-XG-N with varying XG concentrations at varying pressures

3.8 Electrical conductivity

The electrical conductivity of selected carbon microbeads was analyzed using a 4-point measurement technique under different pressures. All the carbon aerogel microbead samples exhibit an electrical conductivity in the range of 1200–1700 S/m at higher pressure. It can be seen from Fig. 7 that the electrical conductivity is increased with increasing pressure as the packing density of the samples is increased. The increase in packing density results in good compaction of the microbeads whereby more paths for transport of electrons are available, which in turn results in good electrical conductivity. The dependence of electrical conductivity with respect to envelope density was previously reported by our group [28]. The electrical conductivities of pH adjusted samples are in the same range (Fig. S19). There is no correlation with the reported conductivity values of the CBs with respect to XG and/or type of gelation bath.

3.9 Mechanical properties

The carbon microbeads were mechanically tested under compressive load. A photograph of the experimental set-up is presented in Fig. S20. The load and the displacement of the test machine pressure punch were monitored. For comparison of the different microbead batches, at least four beads of each batch were tested, and the respective nominal stresses and strains were calculated. Figure 8a shows typical nominal stress-strain curves for CB-1.0XG-H microbeads. The complete set of nominal stress-strain curves for all types of carbon microbeads are presented in Figs. S21–S24. The beads exhibit brittle fracture behavior. During the experiment, the nominal stress-strain curves display several stress drops. The load at the first major stress drop is regarded as nominal fracture stress or strength, respectively. Smaller stress drops are associated with chipping of flakes from the beads. During further displacement of the pressure punch, the bead material is compressed, entailing stress

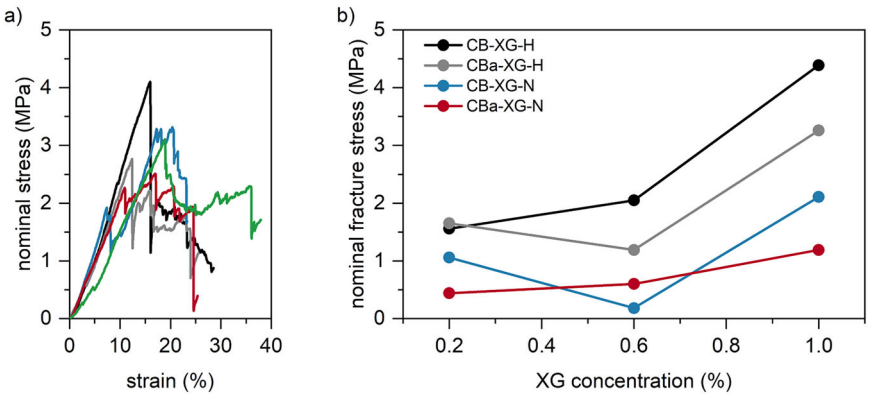

Fig. 8 **a** Nominal stress-strain curves of CB-1.0XG-H (Five beads were tested). **b** Nominal fracture stress derived from median value of load at first fracture (see Table S7) for CB-XG-H and CB-XG-N with and without pH-adjustment

increase until further cracking and associated stress drops. The stress-strain curves of individual beads differ in maximum stress, fracture stress at first major load drop, and strain at fracture stress. For CB-XG-H and CB-XG-N samples with and without pH adjustment, average and median fracture load values as well as average bead diameter and nominal fracture stress are summarized in Table S7. In order to reduce the effect of outliers, which can be huge for data sets with a small number of experiments, the nominal fracture stress for each batch was calculated with the median value of the respective fracture loads. The median values of the fracture load were related to the respective average cross section areas, calculated from the average bead diameter of 100 beads measured for each batch by means of a digital calliper. The nominal fracture stress data of the four batches is presented in Fig. 8b as a function of the wt% of xanthan gum used for preparing the microbeads.

An addition of XG in the range from 0.6 wt% to 1.0 wt% resulted in an increase in nominal fracture stress while XG amounts between 0.2 wt% to 0.6 wt% did not show a clear trend regarding the nominal fracture stress. This finding may be attributed to microstructural changes (compare Section "Micro- and Nanostructure Morphology"), especially to the generation of fibrous appendices which start to form connections between nanoparticles at XG contents of about 0.6 wt%. Such connections may promote the strength of the bead material. Further, the size of the beads is increasing with XG content in non pH adjusted samples but decreasing with XG content in pH adjusted samples. Due to these different trends, the initial pH adjustment may result in no clear trend concerning its effect on the fracture stress. In the case of nitric acid-regenerated batches of beads, the nominal fracture stress is found to be lower in comparison to hydrochloric acid-regenerated batches. This difference is attributed to the different acid concentration used for gelation, which was as low as 0.5 M HNO_3 compared to 2 M HCl as a gelation bath. The HNO_3 concentration had to be that low, since otherwise the pristine RF microbeads were destroyed due to dissolution, nitration, and oxidation by nitric acid during the regeneration process [50]. Although the HNO_3 concentration was kept low, visible cracks and stronger coloration of the beads occurred after drying of the RF microbeads regenerated using HNO_3. Hence, the produced carbon microbeads also show some visible cracks on their surface, which are likely to reduce the fracture stress of the respective beads.

4 Conclusion

Resorcinol-Formaldehyde (RF) and carbon aerogel microbeads were successfully prepared via a dropping method and subsequent pyrolysis. We demonstrated that increasing the viscosity of the RF solutions with the thickening agent, xanthan gum (XG), was crucial in order to preserve the spherical shape of the droplets until gelation solidified the droplets. Increasing the concentration of XG resulted in increasingly fibrous microstructures and thus, increased fracture strength of the beads. XG concentration did not influence the properties of RFB and CB apart from mechanical properties. HS-2D-NLDFT pore size distributions derived from N_2 physisorption revealed the ultramicroporous nature of CB, which was readily reflected in the CO_2 adsorption capacities at 273 and 298 K. Generally, CB produced using HNO_3 as gelation bath, were more microporous than CB produced using HCl as gelation bath. The high CO_2 adsorption capacity (up to 4.57 mmol/g), high electrical conductivity (up to 1700 S/m), and good fracture strength of beads produced with high XG concentration for HCl render CB as a versatile and promising material for multiple applications such as carbon capture technology, or in moving bed or fluidized bed column reactors, electrode materials, etc. The promising potential for scalability with e.g., JetCutter technology further increases the potential and attractiveness of these materials.

Data availability

We declare that the data supporting the findings of this study are available within this paper and also in supporting information.

Supplementary information The online version contains supplementary material available at https://doi.org/10.1007/s10971-026-07224-x.

Acknowledgements We would like to thank Dr. Marion Bartsch and Dr. Klemens Kelm for the discussion. We also wish to thank Mr. Benjamin Ignatzi for the support in carbonization process.

Author contributions TA: methodology, investigation, validation, writing—original draft, writing—review & editing, visualization; SMKM: conceptualization, methodology, investigation, validation, writing—original draft, writing - review & editing, visualization; PN: methodology, validation; RP: methodology, validation; BF: methodology, validation, writing; FK: methodology, validation, writing; MS: project administration, writing—review & editing; RT: project administration, writing—review & editing; BM: conceptualization, project administration, writing—review & editing, supervision.

Funding This work was performed in the context of the projects AeroPROcast, supported by the Federal Ministry for Economic Affairs and Climate Action (BMWK, grant number 03ET1527) and FFAE (Program Directorate traffic of the German Aerospace Center). Open Access funding enabled and organized by Projekt DEAL.

Compliance with ethical standards

Conflict of interest The authors have filed patent applications (DE102021100898.0/EP22701913.0) with respect to the process of making RF and Carbon beads as described in this paper.

References

1. Lee J-H, Park S-J (2020) Recent advances in preparations and applications of carbon aerogels: a review. Carbon 163:1–18. https://doi.org/10.1016/j.carbon.2020.02.073.
2. Antonietti M, Fechler N, Fellinger T-P (2014) Carbon aerogels and monoliths: control of porosity and nanoarchitecture via sol−gel routes. Chem Mater 26:196–210. https://doi.org/10.1021/cm402239e.
3. Zang Z, Chou S, Zhao Q, Nie Y, Xin M, Li Z, Tian J, Li B (2025) A review of the production and application of mesoporous carbon and its potential as an excellent carrier for the adsorptive delivery of compounds. Biochar 7:44. https://doi.org/10.1007/s42773-025-00439-1.
4. Dou Z, Liu L, Yuheng E, Xu Q, Yin S, Liu Z, Wang P, Pang W (2025) Challenges and opportunities in Mesocarbon microbeads: From synthesis to utilization. Fuel 402:136017. https://doi.org/10.1016/j.fuel.2025.136017.
5. Liu Z-G, He X-X, Zhao J-H, Xu C-M, Qiao Y, Li L, Chou S-L (2023) Carbon nanosphere synthesis and applications for rechargeable batteries. Chem Commun 59:4257–4273. https://doi.org/10.1039/D3CC00402C.
6. Chen M, Pan M, Chong Y, Wang J, Long D (2018) Engineering the outermost surface of mesoporous carbon beads towards the broad-spectrum blood-cleansing application. Carbon 130:782–791. https://doi.org/10.1016/j.carbon.2018.01.077.
7. Lei Y, Huang Z-H, Yang Y, Shen W, Zheng Y, Sun H, Kang F (2013) Porous mesocarbon microbeads with graphitic shells: constructing a high-rate, high-capacity cathode for hybrid supercapacitor. Sci Rep 3:2477. https://doi.org/10.1038/srep02477.
8. Liu N, Zhang S, Fu R, Dresselhaus MS, Dresselhaus G (2006) Carbon aerogel spheres prepared via alcohol supercritical drying. Carbon 44:2430. https://doi.org/10.1016/j.carbon.2006.04.032.
9. Qiu J, Li Y, Wang Y, Liang C, Wang T, Wang D (2003) A novel form of carbon micro-balls from coal. Carbon 41:767. https://doi.org/10.1016/S0008-6223(02)00392-5.
10. Yuan M, Cao B, Meng C, Zuo H, Li A, Ma Z, Chen X, Song H (2020) Preparation of pitch-based carbon microbeads by a simultaneous spheroidization and stabilization process for lithium-ion batteries. Chem Eng J 400:125948. https://doi.org/10.1016/j.cej.2020.125948.
11. Ding L, Olesik SV (2003) Carbon microbeads produced through synthesis and pyrolysis of Poly(1,8-dibutyl-1,3,5,7-octatetrayne). Chem Mater 17:2353. https://doi.org/10.1021/cm048781g.
12. Lü Y, Ling L, Wu D, Liu L, Zhang B, Mochida I (1999) Preparation of mesocarbon microbeads from coal tar. J Mater Sci 34:4043. https://doi.org/10.1016/j.jaap.2021.105039.
13. Lu A-H, Li W-C, Matoussevitch N, Spliethoff B, Bönnemann H, Schüth F (2005) Highly stable carbon-protected cobalt nanoparticles and graphite shells. Chem Commun 1:98. https://doi.org/10.1039/B414146F.
14. Parente MJ, Sitharaman B (2023) Synthesis and characterization of carbon microbeads. ACS Omega 8:34034. https://doi.org/10.1021/acsomega.3c05042.
15. Esumi K, Eshima S, Murakami Y, Honda H, Oda H (1996) Preparation of hollow carbon-microbeads from water-in-oil emulsion using amphiphilic carbonaceous material. Coll Surf A 108:113–116. https://doi.org/10.1016/0927-7757(95)03391-2.
16. Alviso CT, Pekala RW, Gross J, Lu X, Caps R, Fricke J (1996) Resorcinol-formaldehyde and carbon aerogel microspheres. MRS Online Proc Libr 431:521. https://doi.org/10.1557/PROC-431-521.
17. Ganesan K, Budtova T, Ratke L, Gurikov P, Baudron V, Preibisch I, Niemeyer P, Smirnova I, Milow B (2008) Review on the production of polysaccharide aerogel particles. Materials 11:2144. https://doi.org/10.3390/ma11112144.
18. Dwivedi C, Kumar A, Ajish JK, Singh KK, Kumar M, Wattal PK, Bajaj PN (2012) Resorcinol-formaldehyde coated XAD resin beads for removal of cesium ions from radioactive waste: synthesis, sorption and kinetic studies. RSC Adv 2:5557. https://doi.org/10.1039/C2RA20054F.
19. Dwivedi C, Kumar A, Juby KA, Kumar M, Wattal PK, Bajaj PN (2012) Preparation and evaluation of alginate-assisted spherical resorcinol–formaldehyde resin beads for removal of cesium from alkaline waste. Chem Eng J 200–202:491. https://doi.org/10.1016/j.cej.2012.06.081.
20. Dwivedi C, Pathak SK, Kumar M, Tripathi SC, Bajaj PN (2013) Removal of cesium by spherical resorcinol–formaldehyde resin beads: Sorption and kinetic studies. J Radioanal Nucl Chem 297:1. https://doi.org/10.1007/s10967-012-2320-y.
21. Overturf IIIGE, Cook R, Letts SA, Buckley SR, McClellan MR, Schroen-Carey D (1995) Resorcinol/formaldehyde foam shell targets for ICF. Fusion Technol 28(5):1803–1808. https://doi.org/10.13182/FST95-A30416.
22. Lambert SM, Overturf IIIGE, Wilemski G, Letts SA, Schoren-Carey D, Cook RC (1997) Fabrication of low-density foam shells from resorcinol–formaldehyde aerogel. J Appl Polym Sci 65:2111–2122.
23. Milow B, Kamal Mohamed SM (2021) Herstellung von monodispersen Aerogelpartikeln, German Patent No.: DE102021100898A1, German Patent and Trade Mark Office.
24. Anklam T (2021) Synthesis and characterization of resorcinol-formaldehyde (RF) and carbon aerogel microbeads by dropping method. Master's Thesis. University of Cologne, Germany.
25. Schwan M, Schettler J, Badaczewski FM, Heinrich C, Smarsly BN, Milow B (2020) The effect of pulverization methods on the microstructure of stiff, ductile, and flexible carbon aerogels. J Mater Sci 55:5861–5879. https://doi.org/10.1007/s10853-020-04397-w.
26. Thommes M, Kaneko K, Neimark AV, Olivier JP, Rodriguez-Reinoso F, Rouquerol J, Sing KSW (2015) Physisorption of gases, with special reference to the evaluation of surface area and pore size distribution (IUPAC Technical Report). Pure Appl Chem 87:1051–1069. https://doi.org/10.1515/pac-2014-1117.
27. Tegethoff M, Briggman KL (2024) Quantitative evaluation of embedding resins for volume electron microscopy. Front Neurosci 18:1286991. https://doi.org/10.3389/fnins.2024.1286991.
28. Kröner J, Platzer D, Milow B, Schwan M (2024) Electrical conductivity of monolithic and powdered carbon aerogels and their composites. Mater Adv 5:8042. https://doi.org/10.1039/D4MA00678J.
29. Job N (2005) Matériaux carbonés poreux de texture contrôlée synthétisés par procédé sol-gel et leur utilisation en catalyse hétérogène. University of Liege, Liege, Belgium.
30. Laskowski J, Milow B, Ratke L (2014) Subcritically dried resorcinol–formaldehyde aerogels from a base–acid catalyzed synthesis route. Micropor Mesopor Mat 197:308–315. https://doi.org/10.1016/j.micromeso.2014.06.031.

31. Mulik S, Sotiriou-Leventis C, Leventis N (2007) Time-efficient acid-catalyzed synthesis of resorcinol–formaldehyde aerogels. Chem Mater 19:6138–6144. https://doi.org/10.1021/cm071572m.
32. Tannert R, Schwan M, Ratke L (2015) Reduction of shrinkage and brittleness for resorcinol-formaldehyde aerogels by means of a pH-controlled sol–gel process. J Supercrit Fluids 106:57–61. https://doi.org/10.1016/j.supflu.2015.06.021.
33. Shen J, Hou J, Guo Y, Xue H, Wu G, Zhou B (2005) Microstructure control of rf and carbon aerogels prepared by sol-gel process. J Sol-Gel Sci Technol 36:131–136. https://doi.org/10.1007/s10971-005-5284-3.
34. Pekala RW (1989) Organic aerogels from the polycondensation of resorcinol with formaldehyde. J Mater Sci 24:3221–3227. https://doi.org/10.1007/BF01139044.
35. Faria S, de Oliveira Petkowicz C, de Morais S, Terrones M, de Resende M, de França F, Cardoso V (2011) Characterization of xanthan gum produced from sugar cane broth. Carbohydr Polym 86:469–476. https://doi.org/10.1016/j.carbpol.2011.04.063.
36. Kuznetsova TS, Burakov AE, Burakova IV, Pasko TV, Dyachkova TP, Mkrtchyan ES, Memetova AE, Ananyeva OA, Shigabaeva GN, Galunin EV (2023) Preparation of a polyaniline-modified hybrid graphene aerogel-like nanocomposite for efficient adsorption of heavy metal ions from aquatic media. Polymers 15:1101. https://doi.org/10.3390/polym15051101.
37. Li J, Wang X, Huang Q, Gamboa S, Sebastian PJ (2006) Studies on preparation and performances of carbon aerogel electrodes for the application of supercapacitor. J Power Sources 158:784–788. https://doi.org/10.1016/j.jpowsour.2005.09.045.
38. Kumar V, Kandasubramanian B (2017) Ionic-liquid-assisted three-dimensional caged silica ablative Nanocomposites. J Appl Polym Sci 134:45328. https://doi.org/10.1002/app.45328.
39. Patil AV, Gurav SR, Sonkawade RG, Vhatkar RS (2024) Unlocking the electrochemical potential of carbon aerogels: tailored performance via controlled carbonization and activation process. Energy 307:132471. https://doi.org/10.1016/j.energy.2024.132471.
40. Wang C, Wang Z, Zhang S, Zhang J, Li K (2023) Ab initio investigation of the adsorption of CO_2 molecules on defect sites of graphene surfaces: role of local vacancy structures. Materials 16:981. https://doi.org/10.3390/ma16030981.
41. Bock V, Emmerling A, Fricke J (1998) Influence of monomer and catalyst concentration on RF and carbon aerogel structure. J Non-Cryst Solids 225:69–73. https://doi.org/10.1016/S0022-3093(98)00060-X.
42. Wolak E, Orzechowska-Zięba A (2024) Change of the surface and structure of activated carbon as a result of HNO_3 modification. Adsorption 30:121–128. https://doi.org/10.1007/s10450-023-00401-2.
43. Repelewicz M, Jedynak K, Choma J (2009) Porous structure and surface chemistry of active carbons modified with inorganic acids. Ochr Środowiska 31:45–50. https://repo.bg.wat.edu.pl/info/article/WAT0a847377843242acb5052ea8659de749/.
44. El-Hendawy AN (2003) Influence of HNO_3 oxidation on the structure and adsorptive properties of corncob-based activated carbon. Carbon 41:713–722. https://doi.org/10.1016/S0008-6223(03)00029-0.
45. Calderon HA, Okonkwo A, Estrada-Guel I, Hadjiev VG, Alvarez-Ramírez F, Robles Hernández FC (2016) HRTEM low dose: the unfold of the morphed graphene, from amorphous carbon to morphed graphenes. Adv Struct Chem Imag 2:10. https://doi.org/10.1186/s40679-016-0024-z.
46. Xie P, Sun W, Du A, Hou Q, Wu G, Fan R (2021) Epsilon-negative carbon aerogels with state transition from dielectric to degenerate semiconductor. Adv Electron Mater 7:2000877. https://doi.org/10.1002/aelm.202000877.
47. Wang X, Zhou J, Xing W, Liu B, Zhang J, Lin H, Cui H (2017) Resorcinol–formaldehyde resin-based porous carbon spheres with high CO_2 capture capacities. J Energy Chem 26:1007–1013. https://doi.org/10.1016/j.jechem.2017.07.010.
48. Patel H, Weldekidan H, Mohanty A, Misra M (2023) Effect of physicochemical activation on CO_2 adsorption of activated porous carbon derived from pine sawdust. Carbon Capture Sci Technol 8:100128. https://doi.org/10.1016/j.ccst.2023.100128.
49. Sun N, Sun C, Liu H, Liu J, Stevens L, Drage T (2013) Synthesis, characterization and evaluation of activated spherical carbon materials for CO_2 capture. Fuel 113:854–862. https://doi.org/10.1016/j.fuel.2013.03.047.
50. King WD, Fondeur FF, Wilmarth WR, Pettis ME, McCollum SW (2006) Reactivity of resorcinol formaldehyde resin with nitric acid. Sep Sci Technol 41:2475–2486. https://doi.org/10.1080/01496390600743151.